# Accepted Manuscript

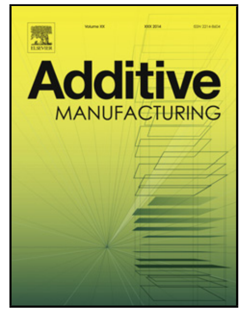


Title: Modeling and control of remelting in high-energy beam additive manufacturing

Author: G. Vastola G. Zhang Q.X. Pei Y.-W. Zhang

PII: S2214-8604(14)00028-1
DOI: http://dx.doi.org/doi:10.1016/j.addma.2014.12.004
Reference: ADDMA 21

To appear in:

Received date: 18-7-2014
Revised date: 5-12-2014
Accepted date: 11-12-2014

Please cite this article as: G. Vastola, G. Zhang, Q.X. Pei, Y.-W. Zhang, Modeling and control of remelting in high-energy beam additive manufacturing, *Additive Manufacturing* (2014), http://dx.doi.org/10.1016/j.addma.2014.12.004

# Modeling and control of remelting in high-energy beam additive manufacturing

G. Vastola, G. Zhang*, Q.X. Pei**, Y.-W. Zhang

*Department of Engineering Mechanics, A*STAR Institute of High Performance Computing, 1 Fusionopolis Way, Connexis #16-16, Singapore 138632*

**Abstract**

Increasing demand for high-quality additive manufactured parts in the aerospace, automotive, medical, and oil&gas industries requires careful control of the part microstructure, residual stress, and density homogeneity. In order to improve part quality, partial remelting of the as-built material during subsequent beam scans is desirable. Here, we make use of computer simulations to explicitly study remelting in laser- or electron beam-melting additive manufacturing. By explicitly implementing phase transformations between the powder, the liquid, and the bulk, we track the amount of material that is subject to remelting. The influence of the beam parameters, such as the beam size, scan speed and power, are investigated and both the cases of an exponential as well as a linear beam absorption profile are considered. We find that, at constant beam cross section, there is an optimal beam shape for remelting. Further, we show how the optimal shape changes when the scan speed is changed and in this case interlayer remelting is also specifically addressed. Calculations are presented for the model case of AISI 316L stainless steel but can be extended to a wide class of metals.

*Keywords:* Powder Metallurgy, Phase transitions, Laser melting, Additive Manufacturing

*PACS:* 81.20.Ev, 64.70.D-, 64.70.kd, 44.35.+c

## 1. Introduction

Monolithic, epitaxial build-up of material in additive manufacturing is a cornerstone for high-quality parts production in the aerospace, marine, oil&gas, and medical industries [1, 2, 3, 4]. In this regard, laser and electron beam melting of powders into the final parts is showing continuous interest due to the high-density, high-strength achievable in the built parts [1]. In order to achieve optimal mechanical properties, a careful control of the part microstructure and homogeneity is necessary. In particular, local remelting of the already built part, and especially of the heat-affected zone [5], is known to increase the part quality

*Corresponding author. Email address: zhangg@ihpc.a-star.edu.sg
**Corresponding author. Email address: peiqx@ihpc.a-star.edu.sg

*Preprint submitted to Elsevier* *December 5, 2014*

in terms of improved material homogeneity [6], reduced density of defects [7], and improved degassing and deoxidation [8]. On the other hand, limited remelting results in poor metallurgical bonding between the newly solidified material and the existing formed shape [9], poor wetting [10], and un-even microstructure distribution [11]. Equally, excessive remelting is also not desirable, as it limits geometrical accuracy in the built part [12]. Moreover, excessive remelting also deteriorates interlayer metallurgical bonding, since it induces a wavy interface between the lower and upper layer of solidified material [13]. Similar to the case of AISI 316L, remelting is important for other materials, as recently demonstrated by Thijs [14] for Selective Laser Melting (SLM) of Tantalum. Also, it is important for Nickel-based superalloys [11], and Ti-6Al-4V [15], where it allows complete degassing and dissolution of low-density inclusions, critical for aerospace-quality Titanium [16], and Aluminum [17]. Beside metals, remelting is important for polyamides because it improves wetting of the liquid in the pores of the solid, improving the part density [18].

The importance of the topic has driven many authors to study melting and remelting in several additive and non-additive welding systems and materials. Yadroitsev *et al.* [19] and Tolochko *et al.* [20] studied SLM of metals using high frame-rate cameras, showing the local phase transformations surrounding the melt pool. Majumdar *et al.* investigated both the mechanical and electrical properties of laser-deposited 316L steel [6]. Koulis *et al.* investigated the case of arc remelting [21], where the melt pool was studied in details using a computational fluid dynamics approach. Rao *et al.* worked on modeling the electro-slag processing of ingots [22], while attention was also given to droplet-deposition of Aluminum [17]. Moreover, laser remelting of die-casting Magnesium alloy was carried out to study the effect on pores formation [23]. For the case of Ti-6Al-4V, a detailed study of the morphological evolution of the melt pool appeared recently with a detailed investigation of heat flow and mass transport within the melt pool [24].

In this paper, we perform Finite Element Method (FEM) calculations of the phase evolution of AISI 316L stainless steel during laser-beam additive manufacturing. We explictly implement the phase changes between powder, liquid and solid and numerically track the evolution of the melt and remelt pool during scanning. We investigate the effect of the beam size and scan speed, at constant heat given to the material, and find that the scan speed has a major impact on the size of the remelt pool. We also find that, at constant beam cross-section, there is an optimal beam size and shape that maximizes the remelt volume fraction. Finally, we show how the optimal remelt pool is affected when the scan speed is changed. Our results suggest a route to predict and control the amount of remelting during scanning, and can be particularly useful as an aiding tool in real manufacturing in order to obtain high-uniformity, low-porosity, high-strength final parts.

## 2. Method

The simulations were performed on a computational domain of $1.8 \times 1.8 \times 0.6$ $mm^3$ in size, assembled using the MSC. Patran ® preprocessor. The domain consisted of 120000 brick elements with a finer mesh

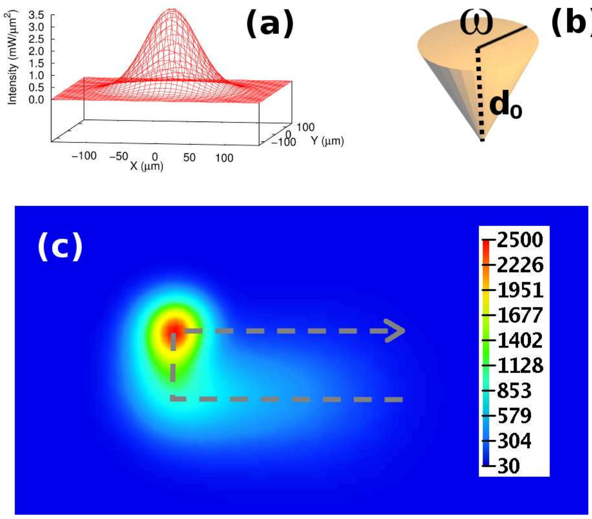


Figure 1: Graphical representation of the intensity of the beam in (a) an horizontal profile and (b) in three-dimensions, where the beam radius $\omega$ and depth $d_0$ are depicted. (c) Top-view of the temperature distribution during the raster turning point of the beam, showing the raster trajectory of the beam in grey. The width and height of the plot are 1500 and 800 $\mu m$, respectively.

of 15 x 15 x 15 $\mu m^3$ elements at the top surface, and gradually coarser towards the lower end of the domain. Boundary conditions were set to 600°C at the lateral boundaries and bottom surface, to model the powder pre-heating during processing. On the other hand, the top surface is the only non-insulated surface. Here, because we are concerned with laser melting, the top surface can exchange heat with the surroundings through both convection and radiation [25]. Therefore, we set the surface heat-exchange coefficient to be 10 $W/mK$ [26] and we implement radiation through the classical Stefan Boltzmann relation, $q = \sigma \left(T^4 - T_0^4\right)$ where $T_0$, the ambient temperature, was also set to 600°C. While these are arbitrary choices, we expect our results not to be qualitatively affected by the exact temperatures we choose [10]. In fact, our primary goal is to be able to reproduce realistic values for the temperature distribution inside the melt pool and powder, as shown for example by Hussein *et al.* [26].

The mechanical and thermal properties for AISI 316L were taken from well-established literature [27]. The presence of powder was considered by scaling the thermal and mechanical properties of the bulk material by the porosity $\phi$, where $\phi$ is a number between 0 and 1. In our calculations, the initial value $\phi = 0.6$ was used [9]. In our model the powder, liquid, and bulk (solid), are considered as three independent phases, each one with individual thermal and mechanical properties. The melting temperature of the solid is set at 1400°C, where for simplicity we disregard the details of the phase transition between solidus and liquidus. The latent heat of fusion was incorporated as a local peak in the specific heat at the melting temperature [26]. For example, with a spot size of 75 $\mu m$ and a penetration depth of 50 $\mu m$, the heat required to melt a volume

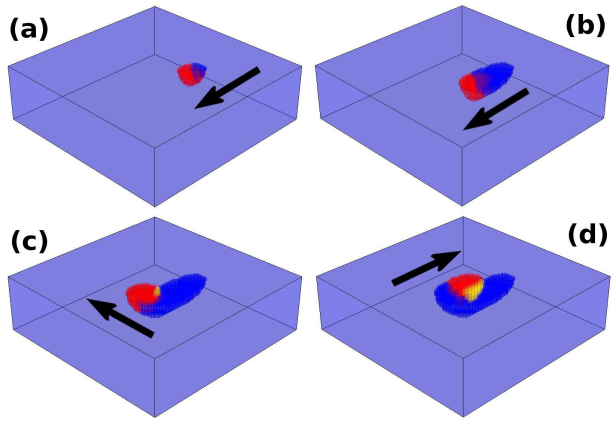


Figure 2: (a)-(d) Sequential snapshots of the phase evolution during raster scan. Liquid elements are depicted in red, bulk elements in dark blue and remelt in yellow. Notice the appearance of remelt at the rastering turning point, and the amount of remelt during the second straight segment of beam scanning. The beam is following the path sketched in Fig. 1(c), and the movement of the beam is shown by the arrows.

of powder corresponding to the spot volume is $\sim 5\times10^{-4}\ J$. The time required for such process is $4.5\ \mu s$, at a laser power of 150 $W$ and absorption efficiency 0.7. Assuming a scan speed of 100 $mm/s$, the time required for the beam to travel across one spot diameter is $\sim 1500\ \mu s$; therefore, such a scan speed is sufficient to achieve full melting of the powder and no incomplete melting is expected using these process parameters.

The laser beam was characterized by a Gaussian in-plane distribution. This shape was chosen because considerable simulations that were carried out previously [28, 26, 29, 30] showed a good agreement with experimental results. Moreover, Gaussian beams are a common setup in industrial-grade laser melting machines [31]. Penetration into the powder was considered with two possible absorption profiles. Specifically, both cases of an exponential as well as a linear absorption were considered [32]. Here, our interest in a linear decay arises because the complex mechanism of energy scattering and absorption through a porous media is still not fully understood, and other authors have reported a linear decay [33]. Beside, a linear profile may be useful for providing qualitative guidelines to the case of electron beam additive manufacturing, where the beam penetration is usually modeled as linear [34]. In summary, the beam energy was considered with both linear and exponential absorption profiles

$$I(x,y,z) = \frac{2AP}{\pi\omega^2} exp^{\left(\frac{-2(x^2+y^2)}{\omega^2}\right)} \left(1 - \frac{z}{d_0}\right) \quad (1) \qquad I(x,y,z) = \frac{2AP}{\pi\omega^2} exp^{\left(\frac{-2(x^2+y^2)}{\omega^2}\right)} exp\left(\frac{-z}{d_0}\right) \quad (2)$$

where $I$ is the beam intensity (in $W/m^2$), $P$ is the laser power, $\omega$ is the beam radius, $d_0$ is the beam penetration depth, and $A$ is the coefficient of absorptivity. The horizontal cross-section and the penetration profile for the case of a linear beam are shown in Figs. 1 (a) and (b), respectively.

Phase transitions were explicitly accounted in our model. This was achieved by adding two extra degrees of freedom (DOF) to every node of our FEM model, where one extra degree of freedom was the local phase and the other was the local porosity. In total, six DOFs were considered on every node, including the displacements along the three directions $u_x, u_y, u_z$ and the local temperature $T$. While the calculation of stresses is part of the model, here we will focus our discussion on the thermal field and distribution of phases. The DOF "phase" could assume three possible values, namely "powder", "liquid" or "bulk". At the same time, the DOF "porosity" was a number between 0 and 1. Phase transitions were modeled by enforcing the following rules: a) if the local phase is powder and the local temperature exceeds the melting temperature, then the local phase in liquid and porosity is 1; b) if the local phase is liquid and the local temperature falls below the melting temperature, the local phase is bulk and porosity is 1; if the local phase is bulk and the local temperature exceeds the melting temperature, the local phase is liquid. This way, rule a) accounts for melting, rule b) for solidification, and rule c) for remelting. Phase evolution was tracked by recording the elements with the majority of nodes belonging to a given phase. The temperature-dependent thermal conductivity and specific heat, as well as the phase transformation rules, were implemented in the form of user subroutines in the software Abaqus ®. Graphical visualization and post-processing was done using the Altair Hyperview ® software.

## 3. Results and discussion

Simulations were run by moving the beam along a raster-type trajectory, as depicted in Fig. 1(c). This trajectory allowed us to study the basic build mechanism of one-layer additive manufacturing. The trajectory comprises of two straight segments with length 600 $\mu m$, connected by a raster turning point, where the hatch spacing was set to 150 $\mu m$. An initial calculation was run with beam radius $\omega = 75$ $\mu m$ and scan speed of 100 mm/s. The laser power was 150 W and the absorptivity 0.7. These numbers were chosen because they are common values in laser melting processing [26], and allowed us to reproduce realistic temperature distributions. The corresponding temperature distribution at the surface is shown in Fig. 1(c), while the phase evolution is shown in Figs. 2(a)-(d), where the liquid elements are colored in red, the bulk is colored in blue, and the remelt is highlighted in yellow. The four snapshots were taken at 1.25, 3.75, 6.5 and 8.75 microseconds, respectively, while the complete movie is provided as Supplementary Data [35]. The phase evolution clearly shows the advancing melt pool, followed by the trail of solid. Because heat is added at the top surface, a strong thermal gradient is present from top to bottom of the melt pool. As a result, solidification starts from the liquid/solid interface at the bottom and propagates towards the top surface. This is consistent with experimental evidence [25]. When the beam reaches the turning point of the raster scan and travels along the hatch spacing, remelting starts to appear. At this point, solidified material is quickly remelt because the beam is spending more time in the region, therefore increasing the local supply

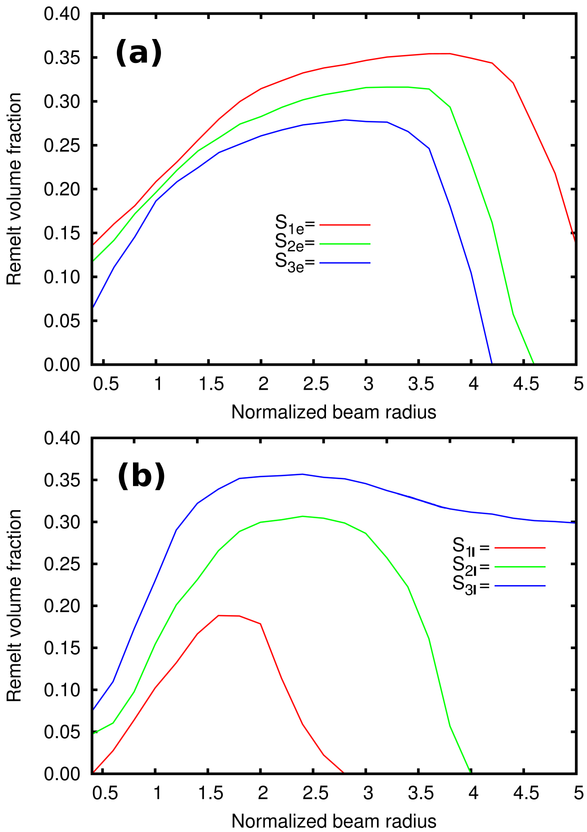


Figure 3: Volume fraction of remelt material during scanning at $100mm/s$, as a function of the beam size, at constant beam cross-section. Calculations are presented for a cross section of 64% (red line), 32% (green line), and 13% (blue line) of the nominal area beam size at $\omega = 75\ \mu m$ (see text for details). Remelt volume fraction is defined as the fraction of material inside the melt pool that comes from remelting. Panel (a) and (b) corresponds to exponential and linear beam penetration profiles, respectively.

of heat to the material. Later, the beam travels the second straight segment and completes the raster scan. Here, remelting is also seen as the consequence of the overlap between the beam local intensity and the material that was solidified after the first line scan. By computing the volume fraction of remelt as the volume of the remelt divided by the volume of the liquid pool, we obtain a remelt volume fraction of $\sim 12\%$. Because the exact amount of remelt volume fraction depends on the beam shape, size and beam speed, we continue by systematically investigating the effect of the beam parameters on the remelt volume for both the cases of an exponential and of a linear absorption into the material. In this study, we focus our attention to the beam rather than to the hatch spacing simply because the hatch has a trivial influence on remelting, namely, the remelt volume fraction monotonically increases as the hatch spacing decreases.

Systematic calculations were run by changing the beam size and depth while keeping the beam cross section $S = \omega d_0$ constant. This way, the beam offers the same cross section to the material, but the beam aspect ratio $r = d_0/2\omega$ can vary. Specifically, the beam radius was considered from 30 to $\omega = 400$ $\mu m$. Our choice of results for comparison at constant cross section area is motivated by the fact that, during raster scan, remelt is primarily controlled by the overlap between the vertical cross-section of the beam and the already solidified material [36]. Volume fraction of remelt material was considered for three indicative values of cross-section $S$, for both cases of exponential and linear decay. For exponential decay, $S = 2\omega d_0$ and, at $\omega = 75$ $\mu m$, $d_0$ was chosen to be 75, 112.5 and 150 $\mu m$ (labels $S_{1e}$, $S_{2e}$, and $S_{3e}$ in Fig. 3(a), respectively). For linear decay, $S = \omega d_0$ and, at $\omega = 75$ $\mu m$, $d_0$ was chosen to be 30, 75 and 120 $\mu m$ (labels $S_{1l}$, $S_{2l}$, and $S_{3l}$ in Fig. 3(b), respectively). While the particular choice of cross-section areas are arbitrary, it allows us to investigate remelting in a range where the penetration depth spans from less than one powder layer to several layers. Results are compiled in Figs. 3 (a) and (b) for exponential and linear decay, respectively, where the beam size was normalized to the hatch spacing. From the figure we can see that the volume fraction of remelt shows a non-uniform dependence upon $\omega$. In particular there is an optimal beam size that maximizes the remelt volume fraction. Initially, volume fraction increases as $\omega$ increases because the beam progressively overlaps with the bulk material solidified during the previous line scan. However, further increase of the beam size results in a decrease in the remelt volume. In fact, as the beam size increases, the beam characteristic volume increases. As a result, the average energy density in the material $(\int_V I dV)/V$ also decreases, effectively limiting the amount of remelt volume at large beam size. We find this result appealing because it shows that a large beam size does not necessarily translates into a large amount of remelt material, even when the hatch spacing is kept constant. For the case of a very small cross-section the corresponding beam volume is small for the entire range of beam sizes. Therefore, energy density is high, resulting in a significant amount of remelt even at large beam sizes. These results tell us that the beam geometry alone is able to profoundly affect the amount of remelt material, influencing the final part quality.

Next, the effect of the beam scan speed was considered. In general, the effect of the beam speed on the temperature distribution inside the material is well documented in literature [24] and will not be further addressed here. However, we mention that the increase of scan speed alone has the general consequence of reducing the thermal gradients during scanning [26] because less heat is given to the material. Here, we change the scan speed while maintaining the same amount of heat given to the material. Following the integration of Eqs. 1 and 2 over the beam volume, we see that a constant heat given to the material requires $P/v$ to be constant. This ratio was kept constant while considering the scan speeds of 100, 200 and 400 $mm/s$. For each of these speeds, systematic calculations were run by varying the beam size in the same range as used before. Results are compiled in Figs. 4 (a) and (b) for exponential and linear absorption, respectively. The figure shows that increasing the scan speed from 100 to 200 $mm/s$ results in an increase of both the maximum amount of remelt volume fraction and of the optimal beam size for remelt. This is consistent with the view that heat accumulation inside the material is in competition with heat removal away from the beam through conduction convection and surface radiation. If the scan speed is high, heat is

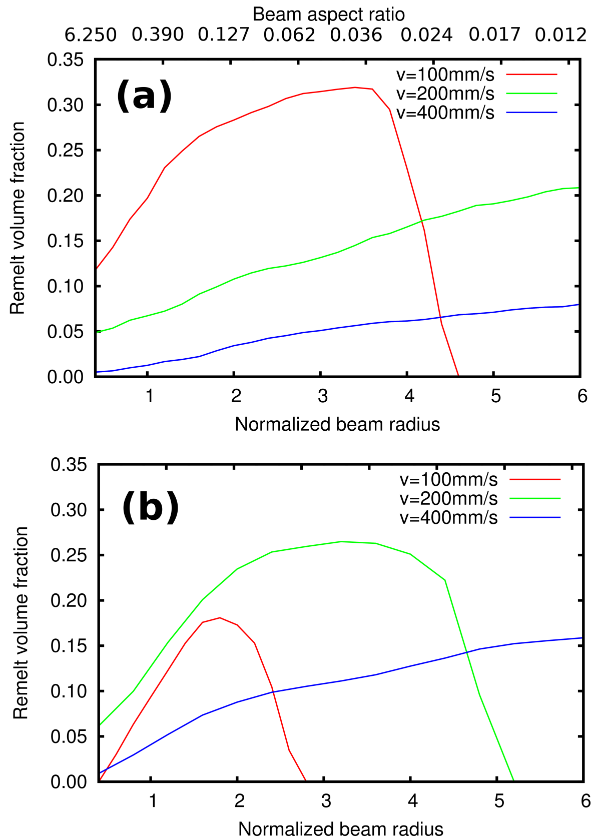


Figure 4: Volume fraction of remelt material as a function of the beam size, where the scan speed is considered at 100 $mm/s$ (red line), 200 $mm/s$ (green line), and 400 $mm/s$ (blue line). The upper axis shows the beam aspect ratio $r$ for the corresponding values of beam size (lower axis). Panel (a) and (b) corresponds to exponential and linear beam penetration profiles, respectively.

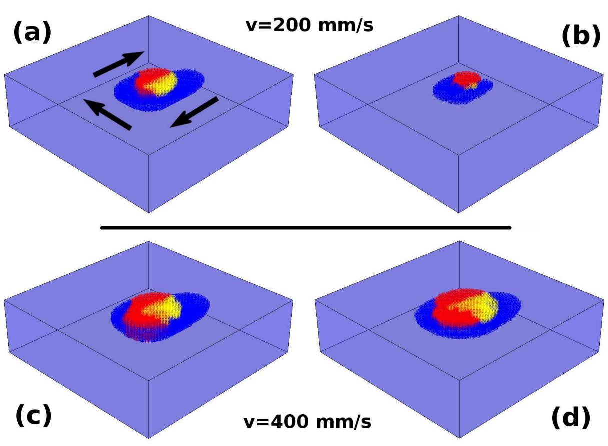


Figure 5: Snapshots of the phase evolution for scan speed of 200 $mm/s$ ((a),(b)) and 400 $mm/s$ ((c),(d)), for an $\omega$ beam size of 250 $\mu m$ ((a),(c)) and 350 $\mu m$ ((b),(d)). At 200 $mm/s$, notice the decrease in the amount of remelt volume as the beam size increase. At 400 $mm/s$, notice the less sensitivity of the remelt volume to the beam size. The arrows in panel (a) depict the raster trajectory of the beam; the trajectory is the same in every panel.

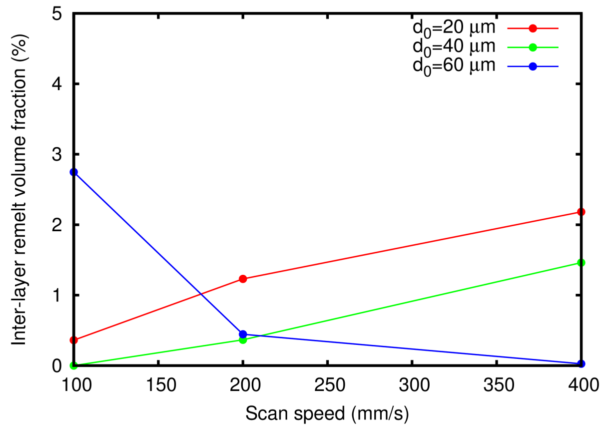


Figure 6: Volume fraction of interlayer remelting during scanning of a powder layer (thickness: 30 $\mu m$) on top of bulk material. The beam spot size is 75 $\mu m$ and the beam penetration profile is exponential with penetration depth of 20 $\mu m$ (red line), 40 $\mu m$ (green line), and 60 $\mu m$ (blue line). Scan speed is changed but the heat given to the material is kept constant.

deposited quickly and the thermal conductivity of the material is not sufficient to carry it away effectively. As a result, local temperature increases, increasing the amount of remelt volume. However, further increase of the scan speed (400 $mm/s$) results in a different behavior, where an optimal beam is not present and the amount of remelt continuously increases with $\omega$ (Fig. 4, blue line). This behavior can be understood with the help of Fig. 5, where snapshots of the corresponding phase evolution are shown. From the figure we see that high scan speed corresponds to a large trail of melt material behind the liquid pool. For this reason, the volume fraction of remelt is lower than the case of smaller scan speed, as shown in Figs. 5(a)-(b). At the same time, increase in the beam size does not induce a decrease of the remelt pool. This is because, contrary to the case of smaller scan speed, here heat is supplied so quickly that considerable melting and remelting occurs even at very large beam volumes. Overall, investigation of the scan speed reveals that by applying the same amount of heat to the material, the amount of remelt material is not intuitively connected to the scan speed.

Moreover, the case of interlayer remelting was investigated, i.e., where the beam is scanning upon a layer of already solidified material. Here, the initial properties of our simulation domain were set to that of bulk material, and one more powder layer (thickness: 30 $\mu m$) was added on top. Interlayer remelt volume fraction was computed as the remelt coming only from the lower layer divided by the volume of the melt pool. Results are compiled in Fig. 6, where the beam had exponential absorption profile, the spot size was 75 $\mu m$, and the heat given to the material was constant. Calculations were repeated at three values of penetration depth $d_0$, namely 20, 40 and 60 $\mu m$. This choice for $d_0$ allows us to investigate both the cases where the penetration depth is smaller and larger than one layer thickness. The calculations show that increasing the scan speed, at constant heat given to the material, increases interlayer remelting at

$d_0 = 20$ and $40\ \mu m$, while decreases at $d_0 = 60\ \mu m$. This is seen as the result of the interplay between a larger penetration depth, which should increase interlayer remelting, and a lower energy density caused by the same increase in penetration depth, which should reduce remelting. These calculations could serve as guidelines for controlling interlayer remelting by carefully choosing the scan speed and the penetration depth.

## 4. Conclusions

In conclusion, a Finite Element Method model was developed to explictly account for the phase transformations of melting, solidification, and remelting during high-energy beam additive manufacturing. Using AISI 316L stainless steel as a model system, we have shown the phase evolution during raster scanning, where remelting begins at the raster turning point. Systematic calculations were performed where the beam spot size was varied while keeping a constant beam cross section, and both the scenarios of an exponential as well as a linear beam penetration depth were considered. Here, it was found that the volume fraction of remelt is linked to the beam size in a complex way. In particular, there is an optimal beam shape that maximizes the remelt volume fraction. At the same time, the beam cross-section area is found to critically influence the remelt volume. In fact, we found that different cross-sections of the beam results in significantly different remelt volumes, indicating that the beam shape has a profound effect on the remelt volume and, ultimately, on the quality of the part.

Investigation of the effect of the beam size, at equal amount of heat supplied to the material, showed that the scan speed is able to influence both the maximal amount of remelt as well as the optimal beam size for remelting. In particular, low scan speed resulted in an optimal remelt volume fraction, while larger scan speeds showed a monotonic increase in remelt, due to the high supply rate of heat into the material. At the same time, explicit study of interlayer remelting showed that high-speed, high-power scanning strategies could enhance interlayer remelting as compared to low-speed, low-power scanning, for powder penetration depths comparable to one layer thickness. Knowledge of this dependence, highlighted in our Fig. 3 and Fig. 4, could be useful as a general guideline to help controlling the amount of remelt material during additive manufacturing. This, is turn, is expected to help the production of high-quality part by improving the material uniformity and, therefore, mechanical properties.

We acknowledge helpful discussions with S.M.L. Nai, Z. He, N. K. Babu and S. Maleksaeedi at A*STAR Singapore Institute of Manufacturing Technology (SIMTech), and X. Tan, Prof. S.B. Tor, S. Yuan, Prof. K. Zhou at Nanyang Technological University. This work was supported by the Agency for Science, Technology and Research of Singapore through the Industrial Additive Manufacturing Program (SERC Grants No: 132 550 4103 and 132 550 4106).

## References


[1] L. Murr, S. Gaytan, D. Ramirez, E. Martine, J. Hernandez, K. Amato, P. Shindo, F. M. R. Wicker, Metal fabrication by additive manufacturing using laser and electron beam melting technologies, J. Mater. Sci. Technol. 28 (2012) 1.

[2] L. Murr, S. Quinones, S. Gaytan, M. Lopez, A. Rodela, E. Martinez, D. Hernandez, E. Martinez, F. Medina, R. Wicker, Microstructure and mechanical behavior of ti6al4v produced by rapid-layer manufacturing, for biomedical applications, J. Mech. Behav. Biomed. Mat. 2 (2009) 20.

[3] A. Mitchell, R. Reed, The influence of remelting processes on the mechanical properties of forged alloys, High Temp. Mat. and Proc. 28 (2009) 285.

[4] L. Li, W. Syed, A. Pinkerton, Rapid additive manufacturing of functionally graded structures using simultaneous wire and powder laser deposition, Virtual and Physical Prototyping 1 (2006) 217–225.

[5] A. Pinkerton, L. Li, Multiple-layer cladding of stainless steel using a high-powered diode laser: an experimental investigation of the process characteristics and material properties, Thin Solid Films 453 (2004) 471–476.

[6] J. D. Majumdar, A. Pinkerton, Z. Liu, I. Manna, L. Li, Microstructure characterisation and process optimization of laser assisted rapid fabrication of 316l stainless steel, Applied Surface Science 247 (2005) 320–327.

[7] J. V. D. Avyle, J. Brooks, A. Powell, Reducing defects in remelting processes for high-performance alloys, JOM 03.

[8] T. Yahata, T. Ikeda, M. Maeda, Deoxidation of molten titanium by electron-beam melting technique, Metall. Trans. B 24 (1993) 599.

[9] Y. Sun, A. Moroz, K. Alrbaey, Sliding wear characteristics and corrosion behaviour of selective laser melted 316l stainless steel, Journal of Materials Engineering and Performance 23 (2014) 518–526.

[10] S. Das, Physical aspects of process control in selective laser sintering of metals, Adv. Engin. Mat. 5 (2003) 701.

[11] S. Hao, X. Zhang, X. Mei, T. Grosdidier, C. Dong, Surface treatment of dz4 directionally solidified nickel-based superalloy by high current pulsed electron beam, Mat. Lett. 62 (2008) 414.

[12] C. Charles, Modelling microstructure evolution of weld deposited ti-6al-4v, Ph.D. thesis, LuleåUniversity of technology (November 2008).

[13] F. Huang, Z. Jiang, X. Liu, J. Lian, L. Chen, Microstructure and properties of thin wall by laser cladding forming, J. Mat. Proc. Technol. 209 (2009) 4970–4976.

[14] L. Thijs, M. M. Sistiaga, R. Wauthle, Q. Xie, J.-P. Kruth, J. Humbeeck, Strong morphological and crystallographic texture and resulting yield strength anisotropy in selective laser melted tantalum, Acta Mat. 61 (2013) 4657.

[15] H. Zhuk, P. Kobryn, S. Semiatin, Influence of heating and solidification conditions on the structure and surface quality of electron-beam melted ti6al4v ingots, J. Mat. Proc. Technol. 190 (2007) 387.

[16] A. Kalinyuk, N. Trigub, V. Zamkov, O. Ivasishin, P. Markovsky, R. Teliovich, S. Semiatin, Microstructure, texture, and mechanical properties of electron-beam melted ti-6al-4v, Mat. Sci. Eng. A 346 (2003) 178.

[17] Y. Chao, L. Qi, H. Zuo, J. Luo, X. Hou, H. Li, Remelting and bonding of deposited aluminum alloy droplets under different droplet and substrate temperatures in metal droplet deposition manufacture, Int. J. Mach. Tools & Manuf. 69 (2013) 38.

[18] J.-P. Kruth, G. Levy, F. Klocke, T. Childs, Consolidation phenomena in laser and powder-bed based layerered manufacturing, Annals of the CIRP 56 (2007) 730.

[19] I. Yadroitsev, I. Yadroitsava, I. Smurov, Strategy of fabrication of complex shape parts based on the stability of single laser melted track, Proc. of the SPIE 7921 (2011) 79210C.

[20] N. Tolochko, S. Mozzharov, I. Yadroitsev, T. Laoui, L. Froyen, V. Titov, M. Ignatiev, Selective laser sintering and cladding of single-component metal powders, Rapid Prototyping Journal 10 (2004) 88–97.

[21] K. Pericleous, G. Djambazov, M. Ward, L. Yuan, P. Lee, A multiscale 3d model of the vacuum arc remelting process, Metall. Mat. Trans. A 44A (2013) 5365.

[22] L. Rao, Q. Hu, X. Li, Numerical simulation study of consumable electrode melting process in electro-slag remelting ingots, Vol. 189 of Advanced Materials Research, Scientific.Net, 2011, Ch. Manufacturing Process Technologies, p. 3895.

[23] X. Wang, G. You, Z. Yang, S. Long, Pore formation mechanism in laser local re-melted areas of die cast magnesium alloy az91d, Acta Metall. Sinica 48 (2012) 1437.

[24] M. Jamshidinia, F. Kong, R. Kovacevic, Numerical modeling of heat distribution in the electron beam melting of ti-6al-4v, J. Manuf Sci Eng. 135 (2013) 061010.

[25] I. Yadroitsev, I. Smurov, Surface morphology in selective laser melting of metal powders, Phys. Proc. 12A (2011) 264.

[26] A. Hussein, L. Hao, C. Yan, R. Everson, Finite element simulation of the temperature and stress fields in single layers built without-support in selective laser melting, Mat. and Design 52 (2013) 638.

[27] K. Mills, Recommended values of thermophysical properties for selected commercial alloy, Woodhead Publishing, 2002.

[28] I. Roberts, C. Wang, R. Esterlein, M. Stanford, D. Mynors, A three-dimensional finite element analysis of the temperature field during laser melting of metal powders in additive layer manufacturing, Int. J. Mach. Tools & Manuf. 49 (2009) 916.

[29] S. Kolossov, E. Boillat, R. Glardon, P. Fischer, M. Locher, 3d fe simulation for temperature evolution in the selective laser sintering process, Int. J. Mach. Tools & Manuf. 44 (2004) 117.

[30] L. Costa, R. Vilar, T. Reti, A. Deus, Rapid tooling by laser powder deposition: process simulation using finite element analysis, Acta Mat. 53 (2005) 3987.

[31] SLM Solutions GmbH, http://stage.slm-solutions.com.

[32] R. McVey, R. Melnychuk, J. Todd, R. Martukanitz, Absorption of laser irradiation in a porous powder layer, J. Laser Appl. 19 (2007) 214–224.

[33] A. Streek, P. Regenfuss, H. Exner, Fundamentals of energy conversion and dissipation in powder layers during laser micro sintering, Phys. Proc. 41 (2013) 851–862.

[34] C. Liu, B. Wu, J. Zhang, Numerical investigation of residual stress in think titanium alloy plate joined with electron beam welding, Metall. Mat. Trans. B 41B (2010) 1129–1138.

[35] Animation of the phase evolution is provided at the address:.

[36] K. Kempen, B. Vrancken, L. Thijs, S. Buls, J. V. Humbeeck, J.-P. Kruth, Lowering thermal gradients in selective laser melting by pre-heating the baseplate, in: Solid Freeform Fabrication Symposium Proceedings, 2013.

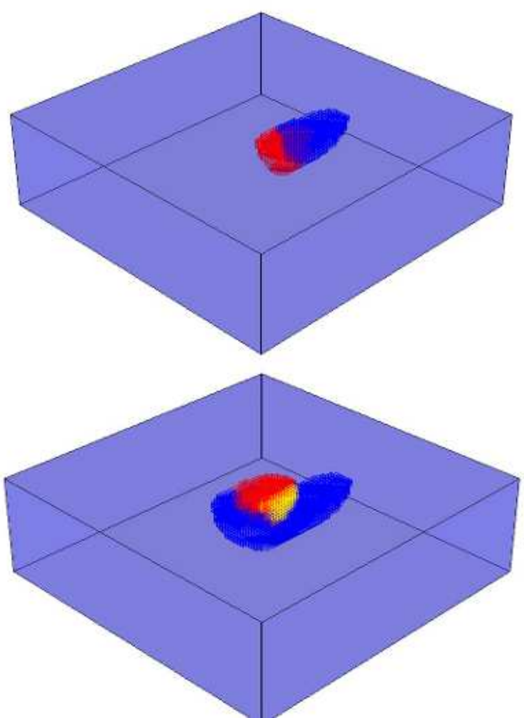

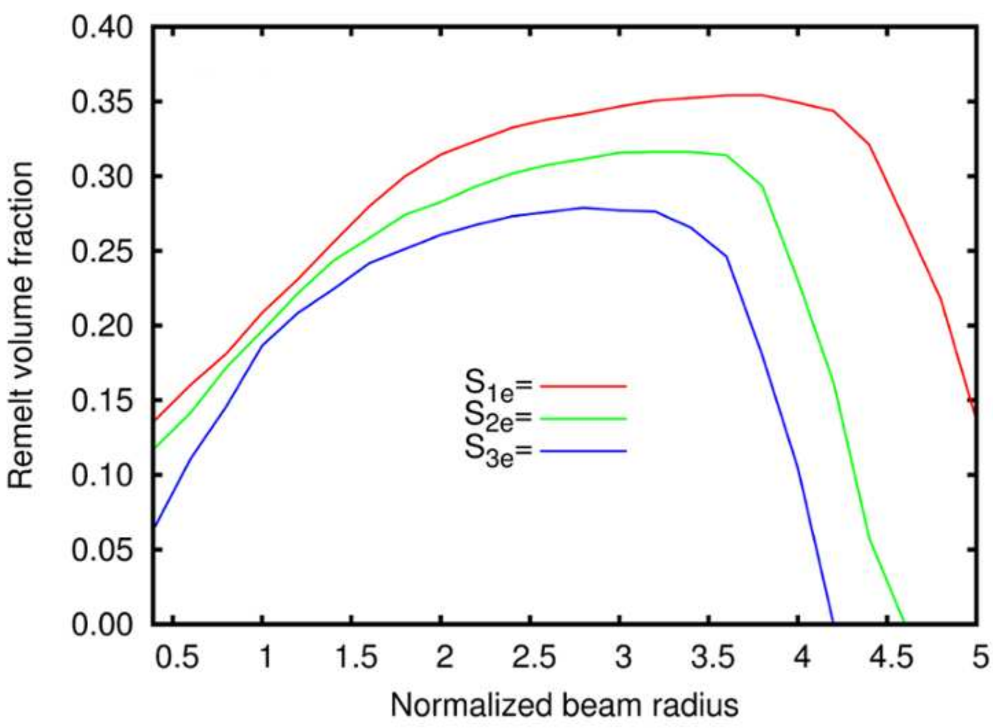
Remelt volume fraction
Normalized beam radius
$S_{1e}$=
$S_{2e}$=
$S_{3e}$=
0.40
0.35
0.30
0.25
0.20
0.15
0.10
0.05
0.00
0.5
1
1.5
2
2.5
3
3.5
4
4.5
5